arXiv:1208.5050v1 [astro-ph.CO] 24 Aug 2012

ACCEPTED FOR PUBLICATION IN THE ASTROPHYSICAL JOURNAL

COMOVING SPACE DENSITY AND OBSCURED FRACTION OF HIGH-REDSHIFT ACTIVE GALACTIC NUCLEI IN THE SUBARU/*XMM-NEWTON* DEEP SURVEY

KAZUO HIROI[1], YOSHIHIRO UEDA[1], MASAYUKI AKIYAMA[2], AND MIKE G. WATSON[3]

Accepted on August 17, 2012

ABSTRACT

We study the comoving space density of X-ray-selected luminous active galactic nuclei (AGNs) and the obscured AGN fraction at high redshifts ($3 < z < 5$) in the Subaru/*XMM-Newton* Deep Survey (SXDS) field. From an X-ray source catalog with high completeness of optical identification thanks to deep optical images, we select a sample of 30 AGNs at $z > 3$ with intrinsic (de-absorbed and rest-frame 2–10 keV) luminosities of $L_X = 10^{44-45}$ erg s^{-1} detected in the 0.5–2 keV band, consisting of 20 and 10 objects with spectroscopic and photometric redshifts, respectively. Utilizing the $1/V_{\rm max}$ method, we confirm that the comoving space density of luminous AGNs decreases with redshift above $z > 3$. When combined with the *Chandra*-COSMOS result of Civano et al. (2011), the density decline of AGNs with $L_X = 10^{44-45}$ erg s^{-1} is well represented by a power law of $(1+z)^{-6.2\pm0.9}$. We also determine the fraction of X-ray obscured AGNs with $N_H > 10^{22}$ cm^{-2} in the Compton-thin population to be $0.54^{+0.17}_{-0.19}$, by carefully taking into account observational biases including the effects of photon statistics for each source. This result is consistent with an independent determination of the type-2 AGN fraction based on optical properties, for which the fraction is found to be 0.59 ± 0.09. Comparing our result with that obtained in the local Universe, we conclude that the obscured fraction of luminous AGNs increases significantly from $z = 0$ to $z > 3$ by a factor of 2.5 ± 1.1.

Subject headings: galaxies: evolution — galaxies: active — X-rays: galaxies — surveys

1. INTRODUCTION

The evolution of active galactic nuclei (AGNs) carries key information for understanding the growth history of supermassive black holes (SMBHs) in galactic centers. Recent X-ray surveys have revealed that luminous AGNs have their number density peak at higher redshifts, $z \sim 2-3$, than less luminous ones (Ueda et al. 2003; Barger et al. 2005; La Franca et al. 2005; Hasinger et al. 2005; Silverman et al. 2008; Ebrero et al. 2009; Yencho et al. 2009; Aird et al. 2010). This behavior is called "down-sizing" or "anti-hierarchical" evolution. These results suggest that present-day massive SMBHs formed in the early epoch of the Universe, compared with less massive ones. A similar evolution is also observed in the star forming history of galaxies (e.g., Cowie et al. 1996; Kodama et al. 2004). This provides a further evidence for the cosmological "co-evolution" scenario of SMBHs and galaxies, which is expected from the tight correlation between a SMBH mass and galactic bulge properties observed in the local Universe (see e.g., Magorrian et al. 1998; Ferrarese & Merritt 2000; Gebhardt et al. 2000).

To elucidate the formation processes of SMBHs, it is very important to reveal the AGN evolution at the high redshifts before the density peak, where the rapid growth of SMBHs took place. Optical/infrared AGN surveys, such as the Sloan Digital Sky Survey, the Canada-France High-z Quasar Survey, and the UKIDSS Large Area Survey, are able to detect very luminous quasars at high redshifts, now up to $z \simeq 7$ (Jiang et al. 2009; Willott et al. 2010; Mortlock et al. 2011), revealing that their space number density has a peak around $z \simeq 2-3$ and shows a rapid decline by 96% from $z = 3$ to $z = 6$ (Richards et al. 2006). Recently, the space density of lower luminosity AGNs has been also investigated from deep optical survey fields (Glikman et al. 2011; Ikeda et al. 2011), although the results are still controversial due to the complexity of the corrections required for incompleteness and contamination. While these optical surveys are useful in detecting unobscured (so-called type-1) AGNs, they inevitably miss the population of obscured (type-2) AGNs, the major class of the AGN population (see e.g., Gilli et al. 2007).

Hard X-ray observations at rest-frame energies above a few keV provide an ideal opportunity to detect obscured AGNs, thanks to their much smaller biases against absorption than the optical band and low contamination from stars in the host galaxies. Silverman et al. (2008) reports that the space density of X-ray-selected luminous AGNs significantly declines at $z > 3$, similar to that of optically-selected QSOs, although they have to assume a completeness correction because the spectroscopic identification rate of the sample is not high ($\sim 50\%$). More recently, Brusa et al. (2009) and Civano et al. (2011) have studied X-ray detected AGNs at $z \gtrsim 3$ from the COSMOS survey (Scoville et al. 2007; Hasinger et al. 2007; Elvis et al. 2009), one of wide and deep multi-wavelength surveys over a continuous area. A decline of the space density above $z \sim 3$ is confirmed for luminous AGNs with intrinsic 2–10 keV luminosities of $\gtrsim 10^{44}$ erg s^{-1}. While the functional shape of this decline is found to be consistent with that of the exponential decline parameterization proposed by Schmidt et al. (1995), which is based on the optically-selected QSOs, it still has a large uncertainty due to the limited sample size. For quantitative comparison with the results obtained in other wavelengths and theoretical models, it is important to establish the shape of the decline from a larger X-ray-selected AGN sample with high completeness.

Another key observational property of AGNs is the type-2 AGN fraction (or more precisely, the distribution of absorption column density), which gives strong constraints on the environments around SMBHs including the obscuring tori and

---

Electronic address: hiroi@kusastro.kyoto-u.ac.jp

[1] Department of Astronomy, Kyoto University, Oiwake-cho, Sakyo-ku, Kyoto, Japan

[2] Astronomical Institute, Graduate School of Science, Tohoku University, Aramaki, Aoba, Sendai, Japan

[3] X-Ray and Observational Astronomy Group, Department of Physics and Astronomy, University of Leicester, University Road, Leicester LE1 7RH, UK

[*] Based in part on data collected at Subaru Telescope, which is operated by the National Astronomical Observatory of Japan.

host galaxies. According to the unified model of AGNs (Antonucci 1993; Urry & Padovani 1995), the classification of AGNs depends only on the viewing angle between the observer and the rotation axis of the torus. It is well known that the type-2 AGN fraction decreases with increasing X-ray luminosity (Ueda et al. 2003; Steffen et al. 2003; La Franca et al. 2005; Hasinger 2008; Ueda et al. 2011), indicating that the simplest unified model with a fixed geometry of tori does not hold. Several authors (e.g., La Franca et al. 2005; Treister & Urry 2006; Hasinger 2008) have furthermore reported that the type-2 fraction increases with redshift, suggesting an evolution of the structures around SMBHs. However, due to difficulties of type classification using photon-limited X-ray data and complex biases against obscuration, the intrinsic type-2 AGN fraction at $z > 3$ has been only poorly investigated.

In this paper, we investigate the evolution of the comoving space density of X-ray-selected luminous AGNs and type-2 fraction at high redshifts ($3 < z < 5$) using the X-ray catalog of Subaru/*XMM-Newton* Deep Survey (SXDS), another wide and deep multi-wavelength survey. The organization of the paper is as follows. Section 2 describes the high-redshift AGN sample used in this study. In section 3, we explain the AGN type classification methods using X-ray or optical data. The results of the comoving space density and type-2 fraction are presented in section 4. Section 5 summarizes the conclusions. Throughout this paper, the cosmological parameters (H_0, Ω_M, Ω_Λ) = (70 km s^{-1} Mpc^{-1}, 0.3, 0.7) are adopted. The "log" symbol represents the base-10 logarithm. Quoted errors denote those at 1σ level.

2. SAMPLE

2.1. *Identification of SXDS AGNs*

The Subaru/*XMM-Newton* Deep Survey (SXDS; Furusawa et al. 2008; Ueda et al. 2008) is one of wide and deep multi-wavelength survey projects covering the radio to X-ray bands. The survey has an unprecedented combination of depth and sky area over a contiguous region of >1 deg^2, centered at R.A. = 02^{h}18^m and Dec. = –05^{d}00^m (J2000). The main aims of the SXDS survey are to explore the nature of extragalactic populations over the whole history of the Universe, the co-evolution of galaxies and SMBHs, and the evolution of the large-scale structure, without being affected by cosmic variance.

XMM-Newton observed the SXDS field in seven pointings, with one deep (nominal exposure of 100 ks) observation in the center surrounded by six shallower (50 ks each) ones, in the 0.2–10 keV band with the European Photon Imaging Camera (EPIC; Strüder et al. 2001; Turner et al. 2001). From the combined images taken by three EPIC cameras (pn, MOS1, and MOS2) with a total area of 1.14 deg^2, Ueda et al. (2008) detected 866, 1114, 645, and 136 X-ray sources with sensitivity limits of 6×10^{-16}, 8×10^{-16}, 3×10^{-15}, and 5×10^{-15} erg cm^{-2} s^{-1} in the 0.5–2, 0.5–4.5, 2–10, and 4.5–10 keV bands, respectively, and with a detection likelihood ≥ 7 (corresponding to a confidence level of 99.91%).

Akiyama et al. (2012, in preparation) summarize the results of the identification of the SXDS X-ray sources detected in the 0.5–2 keV and/or 2–10 keV band within the five combined fields-of-view of the Subaru/Suprime-Cam imaging, using optical and infrared spectroscopic data as well as the deep imaging datasets obtained with UKIRT/WFCAM and Spitzer/IRAC. The 3σ detection limit of the deep R-band image reaches 27.5 magnitude. Thanks to the deep optical image, objects with X-ray to optical flux ratio, $\log(f_X/f_R)$, up to +1.3 can be detected, even for X-ray sources at the deepest X-ray detection limit in the soft X-ray band. The $\log(f_X/f_R)$ distribution of typical AGNs ($-1 < \log(f_X/f_R) < +1$; Akiyama et al. 2000) is well enclosed within the detection limit. Furthermore, the 3σ limit of the B-band image (28.5 magnitude) is deep enough to detect the sharp decline below Lyα of high-redshift objects with red $B-R$ color (>1.0 magnitude) even at the R-band detection limit.

Among the 866 sources detected in the 0.5–2 keV from the whole SXDS field, 781 sources are also covered with the deep Subaru/Suprime-Cam optical images in B-, V-, R-, i-, and z-bands (Furusawa et al. 2008). In this study, we treat these 781 sources located within the overlapping region of the X-ray and deep optical imaging data as a parent sample. Once candidates of Galactic stars, stellar objects that are close to a bright galaxy, and clusters of galaxies are removed, 733 out of the 781 sources are remained as candidates of AGNs. Among them, 586 are spectroscopically identified with intensive optical and near-infrared spectroscopic observations in the field. For the other AGN candidates without spectroscopic identification, their photometric redshifts are estimated on the basis of photometric data in 15 bands covering far-UV to mid-infrared wavelength range. Akiyama et al. (2012) apply HyperZ photometric redshift code (Bolzonella et al. 2000), which determines a photometric redshift via template fitting with χ^2 minimization, using both of galaxy and QSO Spectral Energy Distribution (SED) templates.

In order to reduce the number of AGNs with photometric redshifts significantly different from spectroscopic ones ("outliers"), we apply two additional constraints in addition to the χ^2 minimization, considering the properties of the spectroscopically-identified AGNs. First one is that the objects with stellar morphology in the deep optical images are $z > 1$ broad-line AGNs. Almost all X-ray sources with stellar morphology are identified with type-1 AGNs at $z > 1$ in SXDS. They show bright nuclei and their observed optical lights are dominated by the nuclear components. This criterion may not be applicable to a survey with a deeper X-ray flux limit. Second one is the absolute magnitude range of the galaxy and QSO templates. Considering the absolute magnitude range of spectroscopically-identified type-1 and type-2 AGNs, we limit the z-band absolute magnitude ranges of the galaxy and QSO templates between $-25.0 < M_z < -20.0$ and $-26.5 < M_z < -22.0$, respectively. Further details of the photometric redshift determination are discussed in Akiyama et al. (2012).

The accuracy of the photometric redshifts is examined by comparing them with the spectroscopic ones. The median of $\frac{\Delta z}{(1+z_{\rm spec})}$ is 0.06 for the entire sample. We further examine the accuracy by the normalized median absolute deviation (NMAD; σ_z) following Brammer et al. (2008). For the entire sample, σ_z is 0.104, which is larger than that of the photometric redshift estimations for X-ray-selected AGNs with medium band filters (Cardamone et al. 2010; Luo et al. 2010). The σ_z for type-1 AGNs (0.201) is larger than that for type-2 AGNs (0.095). This is because there is no strong feature in the SEDs of the type-1 AGNs except for the break below Lyα. However, since the break can be covered by the deep optical images for AGNs at $z > 3$, the discrepancy between $z_{\rm spec}$ and $z_{\rm phot}$ is smaller for AGNs at $z > 3$. Regarding the completeness and contamination for the $z > 3$ AGN sample, one AGN at $z_{\rm spec} < 2.9$ shows $z_{\rm phot} > 3.0$. In contrast, five AGNs at $z_{\rm spec} < 2.9$ have $z_{\rm phot} > 3.0$.

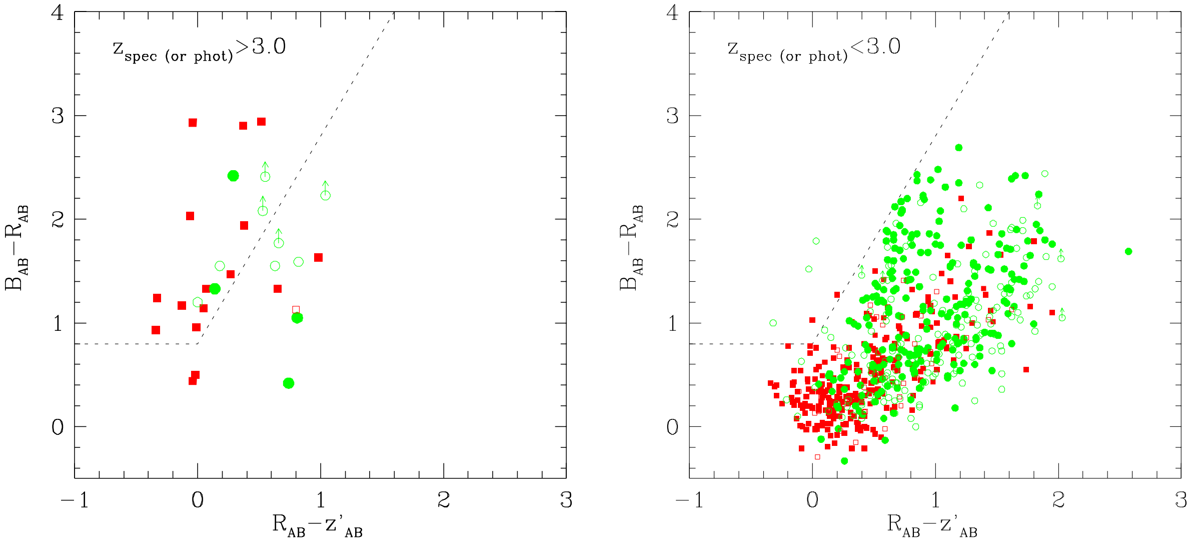

FIG. 1.— Distributions of SXDS AGNs on the $R-z$ and $B-R$ color-color diagram (left: $z > 3$ objects, right: $z < 3$ objects). The red squares and green circles represent type-1 and type-2 AGNs, respectively. AGNs with spectroscopic and photometric redshifts are plotted with filled and open symbols, respectively. The arrows illustrate objects whose $B-R$ colors are their lower limits. The dashed line displays a possible criterion for $z > 3$ AGNs with dropout selection.

It needs to be emphasized that in order to determine photometric redshifts of $z > 3$ AGNs reliably, deep optical imaging data are crucial since they can detect sharp decline of flux below the wavelength of rest-frame Lyα emission. Finally, most of the X-ray sources are identified as AGNs at well estimated redshifts with a very high degree of completeness (99.2%). Photometric redshifts cannot be determined for six objects that are detected in less than 4 bands. We discuss their possible contributions in sections 2.3 and 4.1.

Dropout method is a simple selection criterion for galaxies and AGNs at high redshifts, and sometimes such selection is preferred than the selection with the photometric redshifts, because the photometric redshifts can be affected by a catastrophic failure (Aird et al. 2010). In order to compare the dropout selection with the photometric redshift selection, we plot $R-z$ and $B-R$ color-color diagram for AGNs at $z > 3$ (left) and $z < 3$ (right) in figure 1. The $z > 3$ AGNs show red $B-R$ color, which is consistent with the break below Lyα emission. The red color can be a crude check of the photometric redshifts, which are determined by the SEDs with all 15 bands. Most of the $z > 3$ type-1 AGNs have blue $R-z$ color as well, and they are enclosed within the criterion (dotted lines) that is determined to exclude most of the $z < 3$ AGNs (three $z < 3$ type-2 AGNs that are enclosed within the criterion have photometric redshifts of 2.6–2.8, close to $z = 3$). In contrast, $z > 3$ type-2 AGNs have redder $R-z$ color than type-1 AGNs on average, and some of them have similar colors to AGNs at lower redshifts. Thus, selection based on the optical colors only is useful in general but may miss a part of type-2 AGNs that have red UV color above Lyα emission.

2.2. $z > 3$ *AGN Sample*

For our study, we select a high-redshift AGN sample at $z > 3$ detected in the 0.5–2 keV band, on the basis of spectroscopic and photometric redshifts determined by Akiyama et al. (2012). Thanks to the K-correction effect, even absorbed AGNs can be observed in the 0.5–2 keV band (corresponding to the rest-frame energies above 2–8 keV for $z > 3$), where the maximum sensitivity of *XMM-Newton* is achieved. Our final $z > 3$ AGN sample consists of 30 objects, among which 20 and 10 AGNs have spectroscopic and photometric redshifts, respectively. The properties of the sample are summarized in table 1 and the optical spectra of the spectroscopic sample are displayed in figure 2. Figure 3 exhibits the distribution of redshift for the $z > 3$ AGN sample. Possible effects related to the uncertainties in the photometric redshifts are discussed in the next subsection.

2.3. *Uncertainties of Photometric Redshifts*

Since the photometric redshifts are determined only by broad-band photometries, they could have uncertainties unlike spectroscopic redshifts. Figure 4 illustrates examples of the normalized probability distribution functions (PDFs, P(z)) for the photometric redshift for two sources without spectroscopic redshifts, SXDF0154 and SXDF0321, calculated from the distribution of the χ^2 value obtained in the SED fitting. SXDF0154 has a primary solution (i.e., the highest peak of PDF) at $z > 3$, and hence is included in our $z > 3$ AGN sample. By contrast, SXDF0321 is not included in the sample since the PDF has its peak at $z < 3$. Both of them, however, have finite probabilities at $z < 3$ and $z > 3$.

To take into account the shape of the PDF in each object statistically, we consider the contribution from all 0.5–2 keV selected AGNs in the Akiyama et al. (2012) catalog to the $z > 3$ AGN sample, using the normalized PDFs between $z = 0$ and $z = 5$. For the sources with spectroscopic redshifts, we define their PDFs as delta-functions peaked at their measured redshifts. It is found that the "effective" number of objects in the $z > 3$ AGN sample, computed by summing the fraction of the normalized PDFs in the $z = 3$–5 region ($\int_3^5 P(z)dz$) from all objects, is 30.6, when the six unidentified objects are ignored. This value is almost the same as the number of the best-fit $z > 3$ AGN sample described in the previous subsection. Even if we include the unidentified objects for the calculation, the effective number is computed to be 33.7, which is still within the 1σ error of the number of our $z > 3$ AGN sample. We also confirm that there are no significant changes in the luminosity and absorption column density distributions of the sample when we consider the PDFs of photometric redshifts; here the contribution of each object to the distributions is added with a weight of $P(z)$ over the redshift range of z = 3–5. Hence, we hereafter consider only the best-fit values of the photometric redshifts.

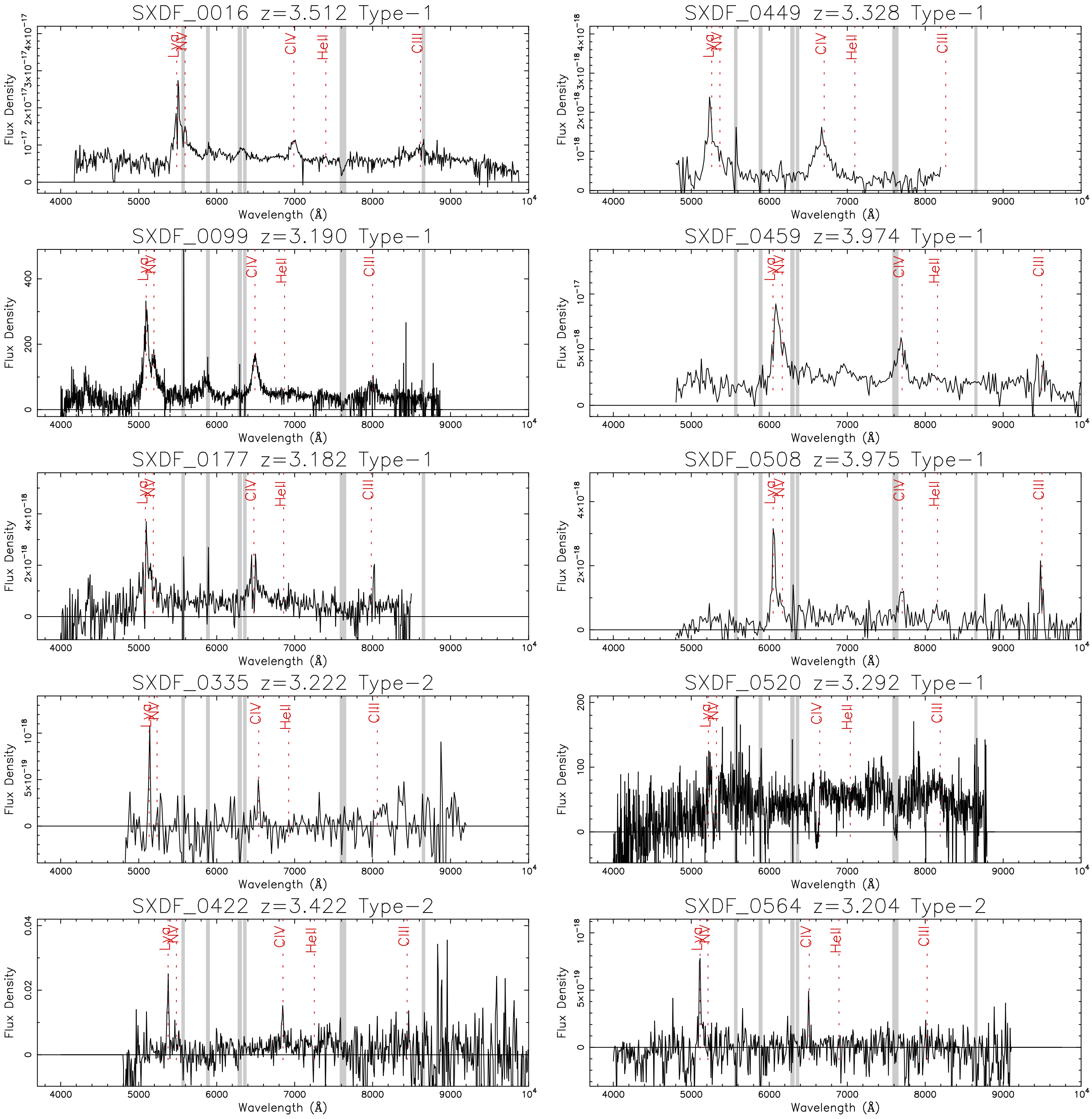

FIG. 2.— Optical spectra of the twenty $z > 3$ AGNs with spectroscopic redshifts. The vertical axis represents the flux density per wavelength (some spectra are not flux-calibrated). The vertical dashed lines in each panel indicate the positions of emission lines typically seen in AGNs. The gray hatched regions exhibit wavelength ranges affected by strong night sky lines or atmospheric absorption lines.

3. ANALYSIS

3.1. *Classification of AGNs*

For our discussion of the obscured AGN fraction, we need to classify each object in our sample as a type-1 or type-2 AGN. There are two different ways to classify AGN: one is based on the optical spectra (optical type) and the other is based on the absorption column densities, $N_{\rm H}$, in the X-ray spectra (X-ray type). The optical type is basically determined by the presence of broad, permitted emission lines. Considering the distribution of the full width at half maximum (FWHM) of the broad-line AGNs in the local universe (Stern & Laor 2012), we classify our spectroscopic sample: those showing significant broad lines with velocity widths larger than 1,000 km s^{-1} are optical type-1 and the others are optical type-2. In the $z > 3$ sample, all but one (SXDF0809) broad-line AGNs have the FWHM of the broad-line width larger than 2,000 km s^{-1}. Thus, their optical classifications are not changed even if we use the threshold of 2,000 km s^{-1} instead of 1,000 km s^{-1}. The CIV line of SXDF0809 has the

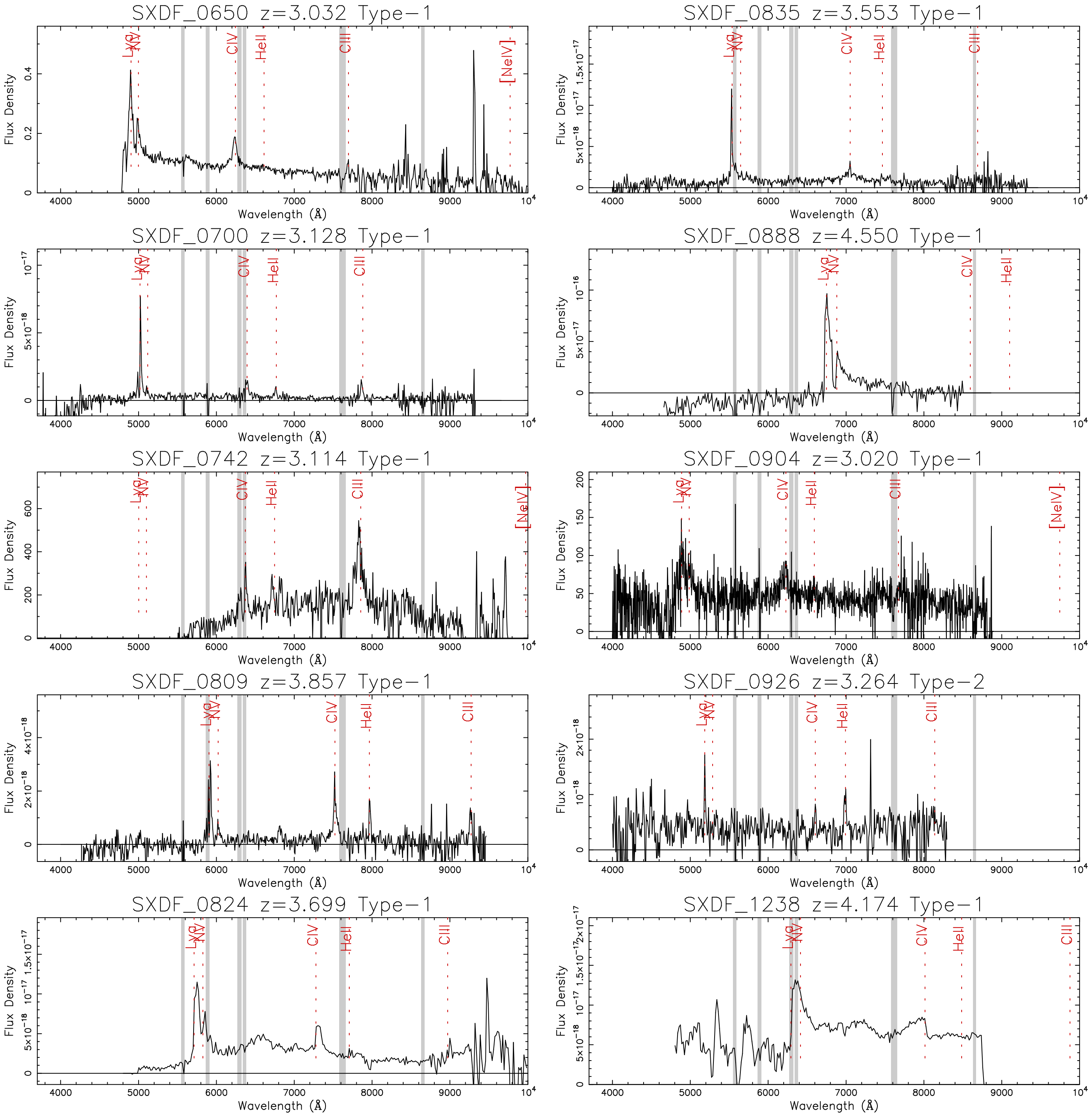

FIG. 2.— *Continued.*

FWHM of 1,470 km s^{-1}. Although it is classified as a type-1 AGN since the CIV line shows broader wing, it needs to be noted that it also shows a strong HeII line, which is typical for narrow-line AGNs. The contribution from the narrow-line component is large in this object.

For the 10 AGNs without spectroscopic redshifts (i.e., those that do not show any significant line features or do not have optical/near-infrared spectra available), we classify them by the type of a template spectrum (i.e., QSO or galaxy). For spectroscopically-identified AGNs, there is a good correlation between the spectral type and the best-fit SED type: type-1 (type-2) AGNs are well fitted with QSO (galaxy) templates. Specifically, among the twenty $z > 3$ AGNs with spectroscopic identification, the spectroscopic and photometric types match well for 15 objects. We therefore classify spectroscopically-unidentified objects fitted better with QSO (galaxy) template into type-1 (type-2) AGNs. Considering the mismatch rate of 25%, we estimate that less than two (= 9*0.25 - 1*0.25) out of the nine AGNs with galaxy spectra could be truly type-1 AGNs; this uncertainty will be taken

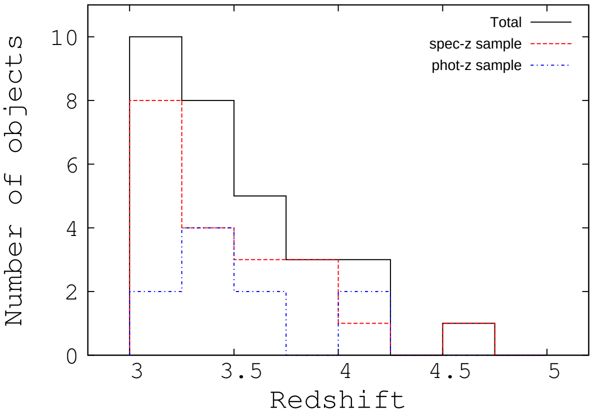

FIG. 3.— Redshift distribution for $z > 3$ AGN sample. Black solid, red dashed, and blue dot-dashed lines represent the total, spectroscopic redshift, and photometric redshift samples, respectively.

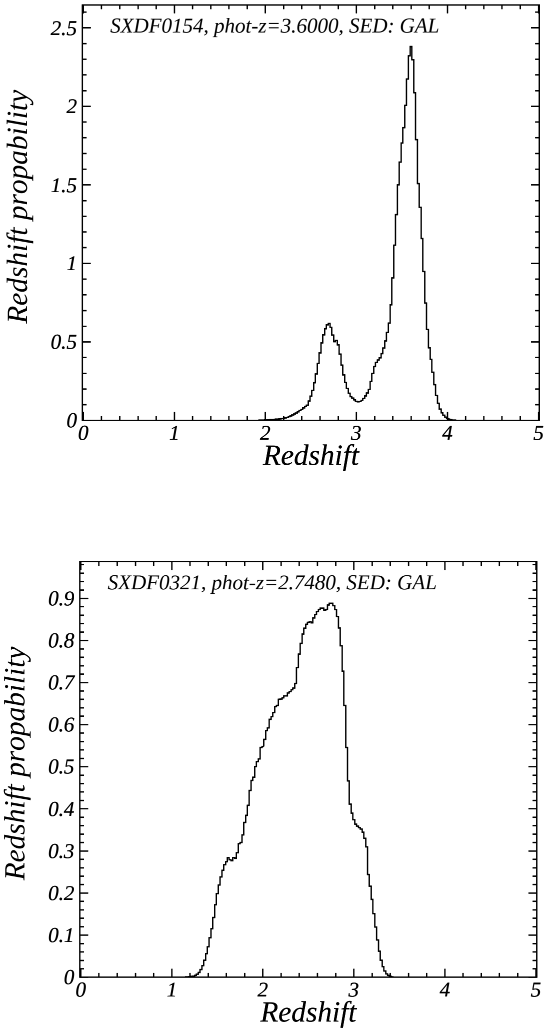

FIG. 4.— Examples of $P(z)$, the probability distribution function for photometric redshift solution (top: SXDF0154, bottom: SXDF0321). Distributions are normalized so that $\int_{z=0}^{5} P(z)dz = 1$.

into account in the discussion on optical type-2 AGN fraction (section 4.2.2). We do not consider combined templates with galaxy and AGN in the photometric redshift determination. It will not affect the classification of the $z > 3$ AGNs, since at $z > 3$ the SXDS sample covers only luminous AGNs and the SEDs of luminous type-1 AGNs are completely dominated by QSO components.

A general problem of relying on the optical type is that the classification may depend on the quality of the available optical spectra, since good signal-to-noise ratio is required to detect less-luminous broad-emission lines on top of stellar continuum emission of host galaxies. Nevertheless, such effects are not expected to be significant in our sample since it consists of luminous AGNs for which contamination from the host galaxies is negligible.

X-ray absorption is an alternative good indicator of AGN type, as expected from the unified scheme (Antonucci 1993; Urry & Padovani 1995) : type-2 AGNs are viewed through the dust torus, and hence have higher absorption column densities than type-1 AGNs. In the present work, we adopt $N_{\rm H} = 10^{22}$ cm^{-2} as the dividing criterion: AGNs with log $N_{\rm H} < 22$ and > 22 are classified as X-ray type-1 and type-2, respectively. This criterion is adopted by many authors, and is known to be generally in good agreement with the optical type (see e.g., Ueda et al. 2003). The merit of using X-ray classification is that observational biases in X-ray surveys can be well defined and can be corrected in a straightforward way. Thus, we basically adopt the X-ray type for our study, although consistency with results based on the optical type is also discussed.

3.2. *Absorption Column Density*

To derive the absorption column density ($N_{\rm H}$) for each AGN, we use an X-ray hardness ratio (HR) between two energy bands, since it is difficult to perform spectral fitting due to the limited photon statistics for most of the X-ray sources in our sample. We define the HR value as

$$\mathrm{HR} = (H-S)/(H+S), \qquad (1)$$

where S and H are the vignetting-corrected count rates [5] in the 0.3–1.0 keV and 1.0–4.5 keV bands, respectively. We find that this choice of bands gives the best sensitivity for the determination of the $N_{\rm H}$ value for $N_{\rm H} \sim 10^{22}$ cm^{-2}, for objects at z = 3–5. Since these count rates are not available in the Ueda et al. (2008) catalog, we re-analyzed the *XMM-Newton* images in these two bands at the fixed source positions, utilizing exactly the same datasets and analysis software as used in Ueda et al. (2008). The relationship between HR and redshift of our AGN sample is shown in figure 5.

Figure 6 shows the relationship between HR and column density at z = 3, 4, and 5. Here and after, we assume a power law with a photon index of 1.9 plus a reflection component from cold matter with a solid angle of 2π as the intrinsic spectrum, following Ueda et al. (2003). We derive the column densities of our AGN sample from the redshift and observed HR value using this relation, and then calculate their intrinsic (de-absorbed and rest-frame 2–10 keV) fluxes and luminosities. Where an observed HR corresponds to log $N_{\rm H} < 20$, we set it to log $N_{\rm H} = 20$. The column density, flux, and luminosity are also summarized in table 1, and the flux distribution is presented in figure 7. Figure 8 displays the relationship between

---

[5] corresponding to those of the pn detector, obtained by dividing the combined pn+MOS1+MOS2 image by the pn-equivalent exposure map; for details see Ueda et al. (2008)

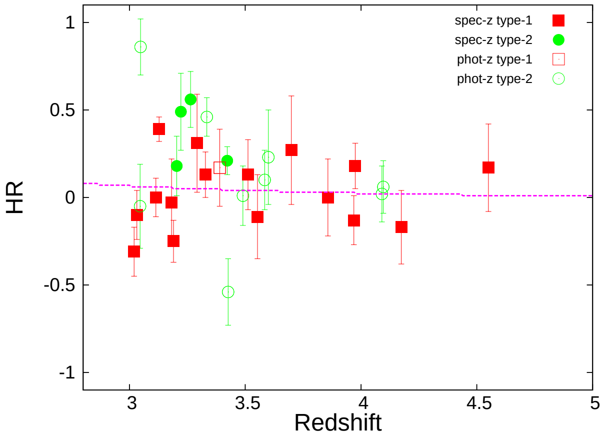

FIG. 5.— Hardness ratio (HR) versus redshift plot for our AGN sample. The red and green symbols correspond to type-1 and type-2 AGNs, respectively. The filled and open circles represent spectroscopic and photometric redshifts samples, respectively. The magenta dashed line corresponds to $\log N_{\rm H} = 22$.

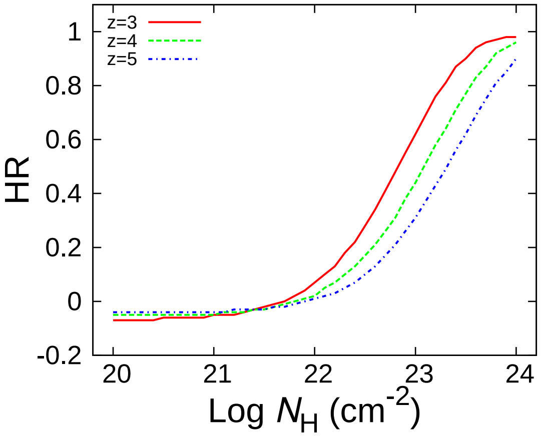

FIG. 6.— The relationship between the hardness ratio HR and absorption column density $N_{\rm H}$. A power law with a photon index of 1.9 plus a reflection component from cold matter with the solid angle $\Omega = 2\pi$ is assumed as the intrinsic spectrum. The red solid, green dashed, and blue dot-dashed lines correspond to the redshifts of 3, 4, and 5, respectively.

the intrinsic luminosity and redshift for our AGN sample. The magenta curves represent the detection limits for AGNs with $\log N_{\rm H} = 20$, 22, and 23, calculated from the 0.5–2 keV count rate at which the survey area becomes one tenth of the maximum value. As noticed from the figure, the survey is incomplete for sources with $\log N_{\rm H} > 23$ in the lowest luminosity range below $\log L_{\rm X} \sim 44.2$ at $z > 3.5$. However, we confirm that this does not affect our estimate on the space density of all Compton-thin AGNs with $\log N_{\rm H} < 24$ over the statistical errors as far as the fraction of heavily obscured AGNs with $N_{\rm H} = 23-24$ is not extremely high. We find that all of our AGN sample have intrinsic luminosities of $\log L_{\rm X} > 44$ erg s^{-1}, and hence belong to the QSO class. While the X-ray AGN types match the optical ones for 18 out of 30 AGNs in our sample, they do not for the others. This is largely due to the statistical error of column density. We can, however, correct for it by considering a conversion matrix from an intrinsic to observed $N_{\rm H}$ distributions (see section 4.2.1).

4. RESULT AND DISCUSSION

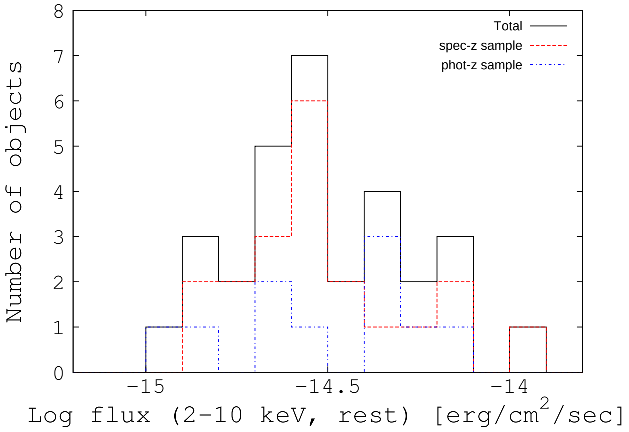

FIG. 7.— Flux distribution for $z > 3$ AGN sample. The definition of the symbols is the same as in figure 3.

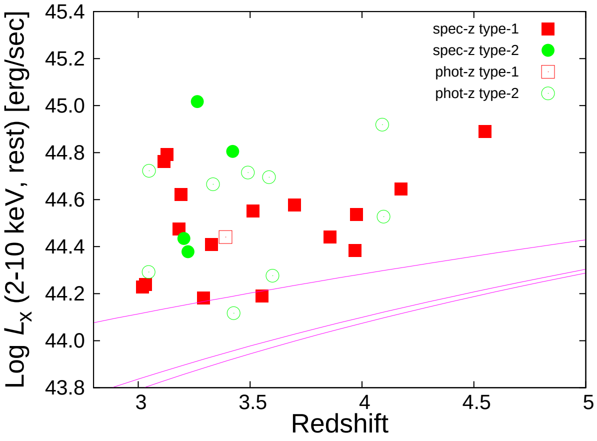

FIG. 8.— Correlation between the intrinsic (de-absorbed and rest-frame 2–10 keV) luminosity and redshift for our AGN sample. The definition of the symbols is the same as in figure 5. The magenta lines represent the detection limits for AGNs with $\log N_{\rm H} = 20$, 22, and 23, from bottom to top, calculated from the 0.5–2 keV count rate corresponding to one tenth of the total survey area.

4.1. *Evolution of the Comoving Space Density of AGNs at $z > 3$*

To investigate the cosmological evolution of AGNs at $z > 3$, we calculate the comoving space density from our sample utilizing the $1/V_{\rm max}$ method (Schmidt 1968). This method takes into account the fact that a fainter source can be found in a smaller volume because of the survey area dependence on flux (or more correctly, count rate). The maximum available volume $V_{\rm max}$ is calculated by the following formula:

$$V_{\rm max} = \int_{z_{\rm min}}^{z_{\rm max}} \Omega(c(L_{\rm X}, z, N_{\rm H}))(1+z)^3 d_A(z)^2 c\frac{d\tau}{dz}(z)dz, \qquad (2)$$

where $\Omega(c(L_{\rm X}, z, N_{\rm H}))$ is the sky coverage at the count rate $c(L_{\rm X}, z, N_{\rm H})$ expected from a source at the redshift z with the intrinsic luminosity $L_{\rm X}$ and the absorption column density $N_{\rm H}$, d_A and $c\frac{d\tau}{dz}$ are the angular distance and the look-back time distance per unit redshift, respectively, both of which are functions of z. Here $z_{\rm min}$ and $z_{\rm max}$ are the lower and the upper edges of the redshift bin used for computing $V_{\rm max}$, respectively. In the present paper, we separate the redshift interval of $3 < z < 5$ into five bins ($z = 3.0$–3.2, 3.2–3.4, 3.4–3.8, 3.8–4.3, and 4.3–5.0), and calculate $V_{\rm max}$ for each AGN in the corresponding

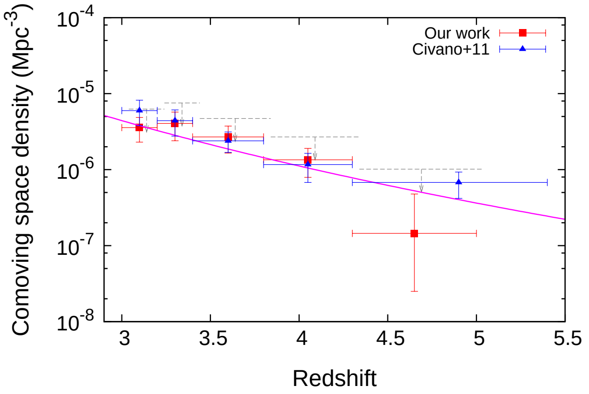

FIG. 9.— Comoving space density of X-ray-selected, luminous AGNs plotted as a function of redshift. The red squares and blue triangles indicate our results at $\log L_X \geq 44$ and those of Civano et al. (2011) at $\log L_X \geq 44.15$, respectively. The errors shown are 1σ. The gray dashed arrows represent the strict upper limits at each redshift bin (for visuality, they are slightly shifted in the x-axis direction), calculated by assuming that all of the unidentified 6 objects are included in the bin. The magenta curve corresponds to the best-fit model fitted to the SXDS data with the form of $(1+z)^{-6.2}$, obtained from the simultaneous fit.

redshift bin. After calculating $V_{\max}$, we sum up the reciprocal value in each redshift bin:

$$\phi = \sum_{i}^{z_{\min}<z<z_{\max}} \left(\frac{1}{V_{\max,i}} \right), \tag{3}$$

where ϕ is the comoving space density in the range $z = z_{\min}$–$z_{\max}$, and i is the index of the sample AGN falling into the redshift bin. The 1σ error is estimated as:

$$\sigma\phi = \sqrt{\sum_{i}^{z_{\min}<z<z_{\max}} \left(\frac{1}{V_{\max,i}} \right)^2}. \tag{4}$$

Where only one source occurs in a given redshift bin, we adopt the Poisson upper and lower limits corresponding to the confidence range of Gaussian 1σ formulated by Gehrels (1986).

Figure 9 displays, as a function of redshift, the comoving space density of AGNs with luminosities $\log L_X$ = 44–45 erg s^{-1} obtained from the SXDS sample (red squares). The gray dashed arrows represent the strict upper limits at each redshift bin, calculated by assuming that all of the unidentified 6 objects are included in the bin. The results from the COSMOS survey (Civano et al. 2011) for AGNs with $\log L_X \geq 44.15$ erg s^{-1} are also plotted for comparison (blue triangles). As can be seen, our results are consistent with those of COSMOS within the statistical errors, indicating a significant decline in the AGN space density from $z = 3$ to higher redshifts.

When we fit the SXDS result with a power-law form of $\propto (1+z)^{p3}$, we obtain $p3 = -7.0 \pm 1.8$. We confirm that the index does not change over the error even when we consider the PDFs of photometric redshifts for all objects including the six unidentified ones (see section 2.3). A simultaneous fit to the SXDS and COSMOS data yields a best-fit slope of $p3 = -6.2 \pm 0.9$, which is shown by the solid magenta curve in figure 9. We find that an exponentially decaying model above a critical redshift $z_{c2} = 2.7$, with the form $10^{p4(z-z_{c2})}$ as adopted by Schmidt et al. (1995), also describes these data well; we obtain $p4 = -0.65 \pm 0.15$ (SXDS only) and $p4 = -0.60 \pm 0.08$ (SXDS+COSMOS). These results on $p3$ or $p4$ give the tightest constraints on the decay profile of the space density of X-ray-selected luminous AGNs with $\log L_X$ = 44–45 erg s^{-1} by utilizing a total of 80 objects. The parameters are little affected by filtering the SXDS sample with $\log L_X \geq 44.15$, the same criterion for the COSMOS sample.

We confirm that the shape of the space-density evolution of X-ray-selected luminous AGNs is consistent with that derived from optical QSO surveys within current uncertainties. With the exponential model, Schmidt et al. (1995) obtained $p4 = -0.43 \pm 0.04$ from optically-selected QSOs with $M_B <$ –26, which roughly corresponds to $\log L_X > 44.5$ assuming a typical SED of QSOs (see e.g., Ueda et al. 2003). More recent results by Richards et al. (2006) give $p4 \simeq -0.67$ for optical QSOs at a magnitude limit of $M_i < -27.6$. Our result ($p4 = -0.60 \pm 0.08$) obtained from X-ray surveys for AGNs with $\log L_X > 44$ lies between the two optical results, as already noted by Brusa et al. (2009). Since X-ray-selected samples contain both type-1 and type-2 AGNs, the same decline profile as that of optically-selected (type-1) QSOs suggests no significant cosmological evolution of the type-2 AGN fraction above $z > 3$, at least in the bright luminosity range. This result is consistent with the conclusion by Hasinger (2008) that the type-2 AGN fraction increases with z but saturates beyond $z = 2$ or $z = 3$.

4.2. *Fraction of Type-2 AGNs at z = 3–5*

To investigate the cosmological evolution of the fraction of type-2 AGNs ($f_{\text{type-2}}$) in the whole Compton-thin population (i.e., with $N_H < 10^{24}$ cm^{-2}) from $z = 0$ to $z = 5$, we constrain $f_{\text{type-2}}$ at z = 3–5 in the intrinsic luminosity range of $\log L_X$ = 44–45 using our SXDS sample. We assume no redshift evolution within the redshift range of z = 3–5, following the previous discussion. There are observational biases in the observed ratio of type-1 and type-2 AGNs, which require careful correction to obtain the true fraction. As mentioned in section 3.1, we primarily adopt the “X-ray type” defined by the absorption seen in the X-ray spectra, for which an evaluation of such biases can be made without assuming a relationship between the optical and X-ray properties. We finally discuss the cosmological evolution of the type-2 AGN fraction by comparing our work with previous results obtained at lower redshifts.

4.2.1. *X-ray Type-2 Fraction*

In our analysis, we consider the two effects. (1) For a given intrinsic luminosity, X-ray type-2 AGNs become less detectable due to the reduction of the observed count rate by photoelectric absorption. (2) Due to the limited number of photons detected, there is a statistical fluctuation of the best-fit column density derived from the observed hardness ratio (i.e., an AGN can apparently have a different absorption column density from the true value). It must be noted that the observed column densities are not simply subject to Gaussian or Poissonian errors but have complex probability distributions with unsymmetric negative and positive errors. This could make the “observed” distribution simply based on the best-fit column density of each object quite different from the “intrinsic” one.

To obtain the true absorption distribution by taking into account these two biases simultaneously, we consider a “conversion matrix” from the intrinsic N_H distribution into the observed one, similar to that used by Ueda et al. (2003). Here we consider the X-ray luminosity function (XLF), the co-moving number density per unit co-moving volume per $\log L_X$ interval as a function of L_X and z, to predict the expected number of AGNs with a given range of $N_{\rm H}$ from the SXDS survey, using the area curve given as a function of count rate (Ueda et al. 2008). Then, by simulating the statistical fluctuation in the observed count rates (and hence hardness ratios) according to the real survey characteristics, we reproduce the expected distribution of the best-fit $N_{\rm H}$ from each input $N_{\rm H}$ value. Finally, we perform a fit to the observed histogram of $N_{\rm H}$ with the model prediction calculated via the matrix, by changing the type-2 fraction as a free parameter. With this procedure, we can most reliably constrain the "intrinsic" absorption distribution in a *statistical* sense, even if it is hard to determine $N_{\rm H}$ of an individual object.

For the shape of the 2–10 keV XLF, we adopt the luminosity-dependent density evolution (LDDE) model of Ueda et al. (2003) by further introducing a power-law decline of the comoving space density at high redshifts as reported in subsection 4.1. Thus, the evolution factor in equation (16) of Ueda et al. (2003) is replaced by the form:

$$e(z,L_{\rm X}) = \begin{cases} (1+z)^{p1} & [z < z_c(L_{\rm X})] \\ (1+z_c)^{p1}\left(\dfrac{1+z}{1+z_c}\right)^{p2} & [z_c(L_{\rm X}) \le z < z_{c2}] \\ (1+z_c)^{p1}\left(\dfrac{1+z_{c2}}{1+z_c}\right)^{p2}\left(\dfrac{1+z}{1+z_{c2}}\right)^{p3} & [z \ge z_{c2}], \end{cases} \tag{5}$$

where $p1$ = 4.23, $p2$ = –1.5, and z_c = 1.9 are adopted, following Ueda et al. (2003). Here the cutoff redshift, beyond which the comoving space density of AGNs decreases, is set to z_{c2} = 2.7, following Schmidt et al. (1995). We adopt $p3$ = –6.2 for the power-law slope at $z > z_{c2}$ based on our result from both the SXDS and COSMOS samples. We also use the "$N_{\rm H}$ function" introduced by Ueda et al. (2003), $f(N_{\rm H})$, i.e. the normalized probability distribution function for the absorption column density. In our calculation, $f(N_{\rm H})$ is assumed to be independent of luminosity and redshift for simplicity. We confirm that the effect caused by the luminosity dependence of the type-2 fraction (e.g., Ueda et al. 2003; Hasinger 2008) on our result is smaller than the statistical uncertainty, because the luminosity range of our sample is narrow (log $L_{\rm X}$ = 44–45).

The expected number of AGNs detected, N, in the intrinsic luminosity range log $L_{\rm X}$ = 44–45, z = 3–5, and intrinsic column density range $N_{\rm H} = N_{\rm H,min}$–$N_{\rm H,max}$ is computed as

$$N = \int_{N_{\rm H,min}}^{N_{\rm H,max}} d\log N_{\rm H} \int_{44}^{45} d\log L_{\rm X} \int_{3}^{5} dz \\ f(N_{\rm H}) \frac{d\Phi(L_{\rm X},z)}{d\log L_{\rm X}} \Omega(c(L_{\rm X},z,N_{\rm H}))(1+z)^3 d_A(z)^2 c \frac{d\tau}{dz}(z). \tag{6}$$

The N values, calculated by assuming a flat $N_{\rm H}$ function, give the relative detection efficiency for AGNs with different column densities. Figure 10 shows the result, normalized to unity at log $N_{\rm H}$ = 20.0–20.5.

Figure 11 illustrates the conversion matrix from the intrinsic to observed $N_{\rm H}$ distributions, calculated for a flat $f(N_{\rm H})$ in the range of log $N_{\rm H}$ = 20–24. Each panel of figure 11 represents the expected $N_{\rm H}$ distribution for AGNs with input intrinsic column densities of log $N_{\rm H}$ = 20–21, log $N_{\rm H}$ = 21–22, log $N_{\rm H}$ = 22–23, and log $N_{\rm H}$ = 23–24. Here, it is again emphasized that the statistical errors in the count rates (eventually, those in the best-fit $N_{\rm H}$ values) are taken into account, based on the observed correlation between the count rate and its error, from the re-analysis described in section 3.2. It is seen from figure 11 that the total number of detected AGNs decreases with the input $N_{\rm H}$ and the observed $N_{\rm H}$ distribution has a wide dispersion with respect to the input $N_{\rm H}$ value due to statistical fluctuations.

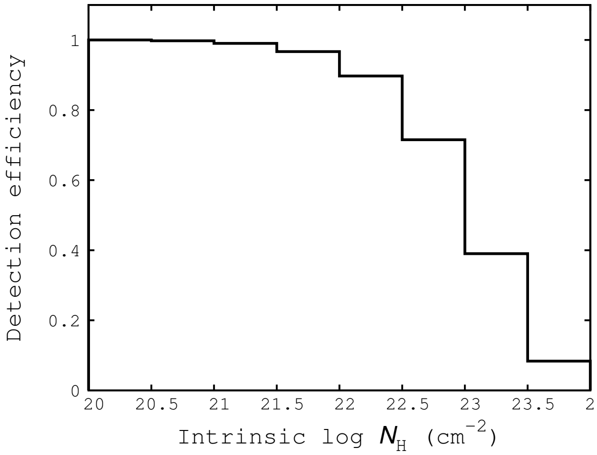

FIG. 10.— Detection efficiency as a function of intrinsic absorption column density, normalized to unity at log $N_{\rm H}$ = 20.0–20.5.

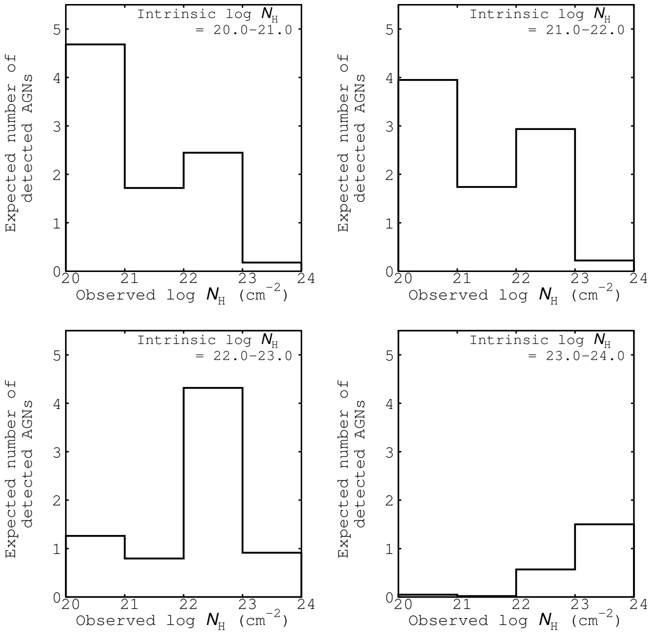

FIG. 11.— Conversion matrix from the intrinsic $N_{\rm H}$ distribution into the observed one. The assumed intrinsic $N_{\rm H}$ distribution is plotted in the top right of each panel.

Using this matrix, we perform a Poisson maximum likelihood fitting to the observed $N_{\rm H}$ histogram of our AGN sample. We assume a flat shape for the $N_{\rm H}$ function in two $N_{\rm H}$ regions, log $N_{\rm H}$ = 20–22 and log $N_{\rm H}$ = 22–24, with the type-2 AGN fraction as a free parameter to be determined through the fitting. The shape of the XLF is fixed to the model described above, while its normalization is tuned to reproduce the total number of observed AGNs at z = 3–5 for our best-fit $N_{\rm H}$ function. It is confirmed, however, that the choice of the XLF model does not affect our conclusion, by introducing the luminosity and density evolution (LADE) model (Aird et al. 2010) instead of the LDDE model. We finally obtain a X-ray type-2 AGN fraction of $0.54^{+0.17}_{-0.19}$ from our sample. Figure 12

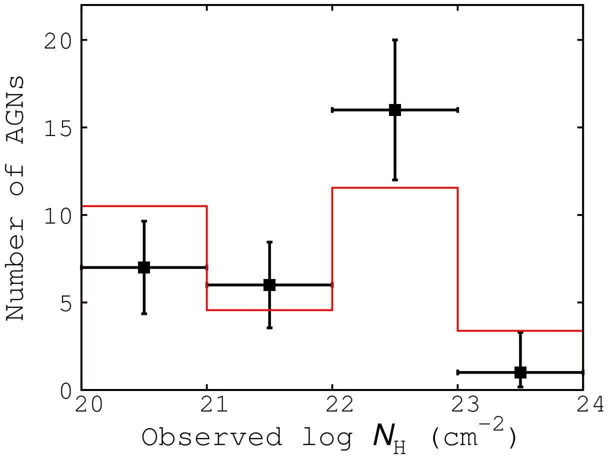

FIG. 12.— Observed histogram of N_H with 1σ Poisson errors (black squares). The red solid line represents the prediction from the N_H function with the best-fit type-2 AGN fraction.

shows the observed histogram of N_H with 1σ Poisson errors (black squares), on which the model prediction from the N_H function with the best-fit type-2 AGN fraction is overplotted (red solid line).

4.2.2. *Optical Type-2 Fraction*

To confirm the result obtained in the previous subsection, here we also estimate the type-2 AGN fraction based on the optical type of each AGN, not by referring to the X-ray absorption. In our sample, we have a total of 17 optical type-1 and 13 optical type-2 AGNs. To derive the intrinsic optical type-2 AGN fraction, we have to assume a relationship between optical type and absorption column density, since the latter determines the observational biases in an X-ray survey. Here, we simply assume that our optical type-1 and type-2 AGNs correspond to those with log $N_H < 22$ and log N_H = 22–24, respectively, following Ueda et al. (2003). Then, we can utilize the detection efficiency plotted in figure 10 to correct for the detection bias. Since the optical properties are independent of the X-ray spectral information, we do not need to consider the statistical error in N_H in contrast with the previous case. In this way, the optical type-2 fraction for AGNs with log L_X = 44–45 erg s^{-1} at z = 3–5 is estimated to be $f_{\rm type-2} = 0.59 \pm 0.09$. Even when we consider the possible uncertainties in the classification of the 10 photometric redshift sample (section 3.1), the type-2 AGN fraction can be at least 0.52 ± 0.09. These values are consistent with the X-ray result. The statistical error becomes smaller than that for the X-ray type-2 fraction because there is no coupling between the two types caused by the statistical fluctuation in the N_H value. We must note, however, that the correspondence of the optical type to X-ray absorption may have some ambiguities that could produce additional systematic uncertainties.

4.2.3. *Evolution of Type-2 Fraction in Luminous AGNs*

By fully taking into account the observational biases, including the photon statistics of the X-ray survey data, we have derived the X-ray type-2 AGN (log $N_H > 22$) fraction in the Compton-thin population to be $0.54^{+0.17}_{-0.19}$ at z = 3–5 and in the luminosity range of log L_X = 44–45. The consistency with the optical type-2 fraction of 0.59 ± 0.09, which is independently measured, supports the robustness of our result. Recently, Masters et al. (2012) roughly estimate the type-2 AGN fraction with log $L_X > 44.15$ at $z \sim 3$–5 to be ∼75%, by comparing the normalizations of X-ray (type-1 + type-2) and UV (type-1 only) luminosity functions derived from the COSMOS data. Their estimate is somewhat larger than our result, although it should be very sensitive to the adopted α_{ox} value used for the luminosity conversion.

We can now compare our X-ray type-2 AGN fraction with that obtained at lower redshifts to investigate its cosmological evolution. Recently, Burlon et al. (2011) have compiled an AGN sample in the local Universe detected in the 3-year Swift/BAT survey performed in the 15–55 keV band, where no detection bias is expected for Compton-thin AGNs (log $N_H < 24$). We find the X-ray type-2 fraction in their sample to be 0.22 ± 0.06 in the luminosity range as corresponding to log L_X = 44–45 in the 2–10 keV band, converted assuming a photon index of 2. Our result at $z > 3$ is significantly higher than the local value, at a ≈90% confidence level based on a χ^2 test, by a factor of 2.5 ± 1.1 (the error is 1σ). When we instead adopt the optical classification for the SXDS sample, the factor becomes 2.7 ± 0.9 and the confidence level corresponds to 99.9%. Thus, we establish the evolution of type-2 fraction from $z = 0$ to $z > 3$ in the high-luminosity range, where it has not been well constrained so far.

We confirm that our results are consistent with the formulation of Hasinger (2008) for the type-2 fraction given as a function of luminosity and redshift. He finds that the type-2 fraction normalized at log L_X = 43.75 (to correct for the luminosity dependence) increases as $(1+z)^{0.62}$ and then saturates above $z \simeq 2$. The formula given in Hasinger (2008) gives

$$f_{\rm type-2} = (-0.11 \pm 0.12) * (\log L_X - 43.75) + (0.578 \pm 0.081) \quad (z = 3.2 - 5.2) \tag{7}$$

By substituting log L_X = 44.6 as the averaged luminosity in our sample, the type-2 fraction is calculated to be 0.49 ± 0.13 at z = 3.2–5.2. Note that Hasinger's "type-2" definition utilizes both optical and X-ray information, which is not exactly the same as ours; in fact, he argues that the criterion roughly corresponds to log N_H = 21.5, instead of 22, and therefore we have to reduce $f_{\rm type-2}$ to match our definition of X-ray type-2 fraction. If we assume a flat N_H function above log N_H = 21.5, the value of type-2 AGN fraction in his definition is reduced by 20% in our definition; specifically, $f_{\rm type-2} = 0.49 \pm 0.13$ in his definition corresponds to an X-ray type-2 fraction of 0.39 ± 0.10 in ours. Thus, the formula of Hasinger (2008) is in agreement with the X-ray type-2 fraction derived from our SXDS sample within the errors, although our results may favor a slightly higher type-2 fraction at $z > 3$.

5. CONCLUSIONS

Thanks to the deep and wide area coverage of the SXDS survey with extensive multi-wavelength follow-up observations, we are able to construct a highly complete X-ray-selected AGN sample at high redshifts ($3 < z < 5$), consisting of 20 and 10 AGNs with spectroscopic and photometric redshifts, respectively. The conclusions are summarized as follows:

- We derive the comoving space density of Compton-thin AGNs at z = 3–5 with intrinsic luminosities of L_X = 10^{44-45} erg s^{-1} at $z > 3$, using the $1/V_{\rm max}$ method. We confirm the trend that the space density significantly declines with redshift as reported in previous works. Combining our SXDS result with that from the COSMOS survey (Civano et al. 2011), we find that the comoving space density decreases as $(1+z)^{-6.2 \pm 0.9}$

or $10^{-(0.60\pm0.08)\times(z-2.7)}$, providing so-far the best constraint on the declining profile of X-ray-selected AGNs at $z > 3$.

- By carefully taking into account observational biases, including statistical uncertainties in the absorption column densities derived from the X-ray data, we derive the obscured AGN fraction with $N_{\rm H} > 10^{22}$ cm^{-2} among those with $N_{\rm H} < 10^{24}$ cm^{-2} to be $0.54^{+0.17}_{-0.19}$ at z = 3–5 in the luminosity range of $L_{\rm X} = 10^{44-45}$ erg s^{-1}. From comparison with the results obtained at lower redshifts, we establish that there is a significant redshift evolution of obscured fraction from z = 0 to $z > 3$ by a factor of 2.5 ± 1.1 in the high-luminosity range.

We thank the anonymous referee for the useful comments that help to improve the clarity of the paper. This work was partly supported by the Grant-in-Aid for JSPS Fellows for young researchers (KH), Scientific Research 23540265 (YU), and by the grant-in-aid for the Global COE Program “The Next Generation of Physics, Spun from Universality and Emergence” from the Ministry of Education, Culture, Sports, Science and Technology (MEXT) of Japan.

REFERENCES

Aird, J., Nandra, K., Laird, E. S., et al. 2010, MNRAS, 401, 2531
Akiyama, M., Ohta, K., Yamada, T., et al. 2000, ApJ, 532, 700
Antonucci, R. 1993, ARA&A, 31, 473
Barger, A. J., Cowie, L. L., Mushotzky, R. F., et al. 2005, AJ, 129, 578
Bolzonella, M., Miralles, J.-M., & Pelló, R. 2000, A&A, 363, 476
Brammer, G. B., van Dokkum, P. G., & Coppi, P. 2008, ApJ, 686, 1503
Brusa, M., Comastri, A., Gilli, R., et al. 2009, ApJ, 693, 8
Burlon, D., Ajello, M., Greiner, J., et al. 2011, ApJ, 728, 58
Cardamone, C. N., van Dokkum, P. G., Urry, C. M., et al. 2010, ApJS, 189, 270
Civano, F., Brusa, M., Comastri, A., et al. 2011, ApJ, 741, 91
Cowie, L. L., Songaila, A., Hu, E. M., & Cohen, J. G. 1996, AJ, 112, 839
Ebrero, J., Carrera, F. J., Page, M. J., et al. 2009, A&A, 493, 55
Elvis, M., Civano, F., Vignali, C., et al. 2009, ApJS, 184, 158
Ferrarese, L., & Merritt, D. 2000, ApJ, 539, L9
Furusawa, H., Kosugi, G., Akiyama, M., et al. 2008, ApJS, 176, 1
Gebhardt, K., Bender, R., Bower, G., et al. 2000, ApJ, 539, L13
Gehrels, N. 1986, ApJ, 303, 336
Gilli, R., Comastri, A., & Hasinger, G. 2007, A&A, 463, 79
Glikman, E., Djorgovski, S. G., Stern, D., et al. 2011, ApJ, 728, L26
Hasinger, G., Miyaji, T., & Schmidt, M. 2005, A&A, 441, 417
Hasinger, G., Cappelluti, N., Brunner, H., et al. 2007, ApJS, 172, 29
Hasinger, G. 2008, A&A, 490, 905
Ikeda, H., Nagao, T., Matsuoka, K., et al. 2011, ApJ, 728, L25
Jiang, L., Fan, X., Bian, F., et al. 2009, AJ, 138, 305
Kodama, T., Yamada, T., Akiyama, M., et al. 2004, MNRAS, 350, 1005
La Franca, F., Fiore, F., Comastri, A., et al. 2005, ApJ, 635, 864
Luo, B., Brandt, W. N., Xue, Y. Q., et al. 2010, ApJS, 187, 560
Magorrian, J., et al. 1998, AJ, 115, 2285
Masters, D., Capak, P., Salvato, M., et al. 2012, arXiv:1207.2154
Mortlock, D. J., Warren, S. J., Venemans, B. P., et al. 2011, Nature, 474, 616
Richards, G. T., Strauss, M. A., Fan, X., et al. 2006, AJ, 131, 2766
Schmidt, M. 1968, ApJ, 151, 393
Schmidt, M., Schneider, D. P., & Gunn, J. E. 1995, AJ, 110, 68
Scoville, N., Aussel, H., Brusa, M., et al. 2007, ApJS, 172, 1
Silverman, J. D., Green, P. J., Barkhouse, W. A., et al. 2008, ApJ, 679, 118
Steffen, A. T., Barger, A. J., Cowie, L. L., Mushotzky, R. F., & Yang, Y. 2003, ApJ, 596, L23
Stern, J., & Laor, A. 2012, MNRAS, 423, 600
Strüder, L., Briel, U., Dennerl, K., et al. 2001, A&A, 365, L18
Treister, E., & Urry, C. M. 2006, ApJ, 652, L79
Turner, M. J. L., Abbey, A., Arnaud, M., et al. 2001, A&A, 365, L27
Ueda, Y., Akiyama, M., Ohta, K., & Miyaji, T. 2003, ApJ, 598, 886
Ueda, Y., Watson, M. G., Stewart, I. M., et al. 2008, ApJS, 179, 124
Ueda, Y., Hiroi, K., Isobe, N., et al. 2011, PASJ, 63, 937
Urry, C. M., & Padovani, P. 1995, PASP, 107, 803
Willott, C. J., Delorme, P., Reylé, C., et al. 2010, AJ, 139, 906
Yencho, B., Barger, A. J., Trouille, L., & Winter, L. M. 2009, ApJ, 698, 380

TABLE 1

PROPERTIES OF OUR HIGH-REDSHIFT AGN SAMPLE.

SXDF ID	R.A. (deg)	Dec. (deg)	Optical Type[a]	SED Model[b]	$z^{[c]}$	$z_{\mathrm{spec}}^{[c]}$	$z_{\mathrm{phot}}^{[c]}$	Count Rate (counts ks^{-1}) 0.5–2	0.3–1.0	1.0–4.5	HR[d]	log N_{H}[e]	Flux[f]	L_{X}[g]
0016	33.93335	-4.92384	1	1	3.512	3.512	3.298	1.40 ± 0.36	0.93 ± 0.29	1.22 ± 0.34	0.13 ± 0.20	$22.30^{+0.41}_{-2.30}$	3.16	3.57
0099	34.08598	-5.28820	1	1	3.190	3.190	3.154	2.38 ± 0.47	3.16 ± 0.51	1.89 ± 0.38	-0.25 ± 0.12	$20.00^{+0.00}_{-0.00}$	4.68	4.19
0154	34.14188	-4.90640	0	2	3.600	...	3.600	0.64 ± 0.20	0.39 ± 0.19	0.63 ± 0.20	0.23 ± 0.27	$22.55^{+0.44}_{-1.27}$	1.58	1.89
0177	34.16076	-5.17883	1	2	3.182	3.182	3.282	1.66 ± 0.33	0.96 ± 0.32	0.90 ± 0.34	-0.03 ± 0.25	$21.44^{+0.99}_{-1.44}$	3.35	2.98
0179	34.16469	-4.72107	0	2	3.426	...	3.426	0.63 ± 0.20	1.34 ± 0.25	0.40 ± 0.20	-0.54 ± 0.19	$20.00^{+0.00}_{-0.00}$	1.23	1.31
0284	34.24511	-4.81274	0	2	3.046	...	3.046	1.22 ± 0.30	0.87 ± 0.28	0.79 ± 0.27	-0.05 ± 0.24	$21.10^{+1.24}_{-1.10}$	2.44	1.96
0287	34.24634	-4.83036	0	2	4.090	...	4.090	2.55 ± 0.42	1.60 ± 0.36	1.65 ± 0.37	0.02 ± 0.16	$21.98^{+0.57}_{-1.98}$	5.12	8.30
0335	34.27461	-5.22714	2	2	3.222	3.222	3.054	0.76 ± 0.18	0.26 ± 0.14	0.75 ± 0.14	0.49 ± 0.22	$22.88^{+0.31}_{-0.34}$	2.60	2.39
0342	34.28106	-4.56844	0	2	3.048	...	3.048	0.88 ± 0.18	0.09 ± 0.10	1.11 ± 0.19	0.86 ± 0.16	$23.40^{+0.60}_{-0.27}$	6.57	5.28
0385	34.32280	-5.08699	0	1	3.390	...	3.390	1.13 ± 0.25	0.58 ± 0.21	0.83 ± 0.23	0.17 ± 0.22	$22.38^{+0.40}_{-1.33}$	2.66	2.76
0422	34.34430	-5.39438	2	2	3.422	3.422	1.840	2.46 ± 0.15	1.52 ± 0.21	2.33 ± 0.25	0.21 ± 0.08	$22.47^{+0.15}_{-0.19}$	6.02	6.38
0449	34.35595	-4.98441	1	1	3.328	3.328	3.038	1.13 ± 0.19	0.78 ± 0.15	1.02 ± 0.18	0.13 ± 0.13	$22.26^{+0.28}_{-0.53}$	2.58	2.56
0459	34.36505	-5.28871	1	1	3.969	3.969	3.946	0.84 ± 0.17	0.71 ± 0.13	0.55 ± 0.12	-0.13 ± 0.14	$20.00^{+1.89}_{-0.00}$	1.60	2.42
0489	34.38058	-5.09214	0	2	3.334	...	3.334	1.43 ± 0.22	0.61 ± 0.15	1.65 ± 0.23	0.46 ± 0.11	$22.86^{+0.16}_{-0.16}$	4.65	4.63
0508	34.39336	-5.08771	1	1	3.975	3.975	4.164	0.98 ± 0.18	0.71 ± 0.14	1.02 ± 0.18	0.18 ± 0.13	$22.53^{+0.26}_{-0.41}$	2.27	3.45
0520	34.39922	-4.70872	1	1	3.292	3.292	2.988	0.58 ± 0.17	0.27 ± 0.14	0.51 ± 0.17	0.31 ± 0.28	$22.62^{+0.42}_{-0.72}$	1.57	1.52
0564	34.43107	-4.54404	2	2	3.204	3.204	2.944	1.25 ± 0.27	0.78 ± 0.23	1.12 ± 0.23	0.18 ± 0.17	$22.36^{+0.31}_{-0.58}$	3.01	2.72
0650	34.49477	-5.13762	1	1	3.032	3.032	2.708	1.10 ± 0.14	0.87 ± 0.15	0.71 ± 0.16	-0.10 ± 0.14	$20.00^{+1.90}_{-0.00}$	2.18	1.73
0700	34.52910	-5.06942	1	2	3.128	3.128	2.986	2.39 ± 0.09	1.02 ± 0.14	2.34 ± 0.19	0.39 ± 0.07	$22.71^{+0.10}_{-0.11}$	7.22	6.18
0742	34.56485	-5.40081	1	1	3.114	3.114	1.360	3.30 ± 0.43	2.55 ± 0.38	2.53 ± 0.37	-0.00 ± 0.11	$21.70^{+0.46}_{-1.70}$	6.84	5.78
0788	34.59990	-5.10029	0	2	4.096	...	4.096	1.00 ± 0.13	0.63 ± 0.13	0.71 ± 0.16	0.06 ± 0.15	$22.19^{+0.43}_{-2.19}$	2.07	3.37
0809	34.61807	-5.26411	1	2	3.857	3.857	3.504	0.98 ± 0.23	0.66 ± 0.21	0.66 ± 0.21	-0.00 ± 0.22	$21.81^{+0.78}_{-1.81}$	1.96	2.76
0824	34.63105	-4.73291	1	1	3.699	3.699	3.766	1.15 ± 0.35	0.50 ± 0.26	0.87 ± 0.36	0.27 ± 0.31	$22.65^{+0.48}_{-1.38}$	2.95	3.77
0835	34.64068	-5.28748	1	1	3.553	3.553	3.210	0.69 ± 0.18	0.48 ± 0.16	0.38 ± 0.14	-0.11 ± 0.24	$20.00^{+2.31}_{-0.00}$	1.34	1.55
0888	34.68521	-4.80691	1	1	4.550	4.550	3.598	1.66 ± 0.43	0.97 ± 0.38	1.35 ± 0.43	0.17 ± 0.25	$22.62^{+0.47}_{-2.62}$	3.72	7.76
0904	34.69847	-5.38866	1	1	3.020	3.020	2.852	1.09 ± 0.20	1.05 ± 0.17	0.55 ± 0.15	-0.31 ± 0.14	$20.00^{+0.00}_{-0.00}$	2.16	1.69
0926	34.72080	-5.01810	2	1	3.264	3.264	1.894	2.91 ± 0.47	0.79 ± 0.35	2.80 ± 0.42	0.56 ± 0.16	$22.99^{+0.23}_{-0.23}$	10.90	10.40
0930	34.72563	-5.52342	0	2	3.490	...	3.490	2.28 ± 0.41	1.35 ± 0.35	1.37 ± 0.29	0.01 ± 0.17	$21.83^{+0.59}_{-1.83}$	4.67	5.19
1032	34.80911	-5.17238	0	2	3.584	...	3.584	1.91 ± 0.39	1.28 ± 0.34	1.56 ± 0.32	0.10 ± 0.17	$22.23^{+0.40}_{-2.23}$	4.19	4.96
1238	35.09164	-5.07500	1	2	4.174	4.174	3.466	1.37 ± 0.35	1.25 ± 0.32	0.89 ± 0.32	-0.17 ± 0.21	$20.00^{+2.10}_{-0.00}$	2.60	4.42

[a] 0: photometric redshift AGNs, 1: optical type-1 AGNs, and 2: optical type-2 AGNs

[b] SED models used for the calculations of photometric redshifts: 1; QSO template and 2; Galaxy template

[c] Chosen redshift; spectroscopic redshift; photometric redshift

[d] Hardness ratio defined as “HR = $(H+S)/(H-S)$”, S: 0.3–1.0 keV count rate and H: 1.0–4.5 keV count rate

[e] The absorption column density in units of cm^{-2}.

[f] The intrinsic (de-absorbed and rest-frame 2–10 keV) flux in units of 10^{-15} erg cm^{-2} s^{-1}.

[g] The intrinsic (de-absorbed and rest-frame 2–10 keV) luminosity in units of 10^{44} erg s^{-1}.